Nanoscale

PAPER

View Article Online
View Journal | View Issue



Cite this: *Nanoscale*, 2022, **14**, 15832

# Microfluidic-assisted biomineralization of CRISPR/Cas9 in near-infrared responsive metal–organic frameworks for programmable gene-editing†

Xiaoyu Xu,‡[a,b,c] Chang Liu,‡[b] Shengyi Wang,‡[a,b,c] Ermei Mäkilä,[d] Jiali Wang,[a,c] Oliver Koivisto,[b] Junnian Zhou,[b,e] Jessica M. Rosenholm,[b] Yilai Shu*[a,c] and Hongbo Zhang *[b,f,g]

Ribonucleoprotein (RNP) based CRISPR/Cas9 gene-editing system shows great potential in biomedical applications. However, due to the large size, charged surface and high biological sensitivity of RNP, its efficient delivery with precise control remains highly challenging. Herein, a microfluidic-assisted metal–organic framework (MOF) based biomineralization strategy is designed and utilized for the efficient delivery and remote regulation of CRISPR/Cas9 RNP gene editing. The strategy is realized by biomimetic growing of thermo-responsive EuMOFs onto photothermal template Prussian blue (PB). The RNP is loaded during MOFs crystallization in microfluidic channels. By adjusting different microfluidic parameters, well-defined and comparable RNP encapsulated nanocarrier (PB@RNP-EuMOFs) are obtained with high loading efficiency (60%), remarkable RNP protection and NIR-stimulated release capacity. Upon laser exposure, the nanocarrier induces effective endosomal escape (4 h) and precise gene knockout of green fluorescent protein by 40% over 2 days. Moreover, the gene-editing activity can be programmed by tuning exposure times (42% for three times and 47% for four times), proving more controllable and inducible editing modality compared to control group without laser irradiation. This novel microfluidic-assisted MOFs biomineralization strategy thus offers an attractive route to optimize delivery systems and reduce off-target side effects by NIR-triggered remote control of CRISPR/Cas9 RNP, improving the potential for its highly efficient and precise therapeutic application.

Received 25th July 2022,
Accepted 11th October 2022

DOI: 10.1039/d2nr04095f

rsc.li/nanoscale



## 1. Introduction

The CRISPR/Cas9 (clustered regularly interspaced short palindromic repeat (CRISPR) associated proteins 9) is a powerful tool for the field of gene manipulation.[1,2] It simplifies the procedure of gene editing by utilizing a single-guide RNA (sgRNA) to recognize target DNA, and then using the endonuclease Cas9 protein to introduce site specific double-strand breaks (DSBs) at target gene site.[3] Successful gene-editing activities have been obtained by using either CRISPR/Cas9 DNA (plasmid DNA and viral genome that can encode Cas9), mRNA, or protein.[4,5] In general, the direct delivery of the Cas9/sgRNA RNP complex is the most widely performed method in recent years due to its fast action, high gene editing efficiency, low off-target effects and immune responses.[6] However, for all the advantages of RNP-based therapeutics, there continues to be some challenges. Currently, physical approaches (electroporation, microinjection, *etc.*) and viral vectors (adenovirus, adeno-associated virus, *etc.*) are still the primary delivery strategies.[7,8] Although some non-viral based nanocarriers, such as DNA nanoclews,[9] cationic lipids or polymers,[10] and black phosphorus[11] have been reported for RNP delivery, they still remain elusive to achieve effective gene-editing both *in vitro* and *in vivo*. In general, there are three delivery problems that need to be considered. Firstly, the CRISPR/Cas9 RNP is large in size and has a highly charged surface, making it difficult to be condensed into small size or encapsulated.[12] Simultaneously, they are sensitive and easily denatured.

[a]*ENT Institute and Department of Otorhinolaryngology, Eye & ENT Hospital, State Key Laboratory of Medical Neurobiology, Institutes of Biomedical Sciences, Fudan University, Shanghai 200031, China. E-mail: yilai_shu@fudan.edu.cn*
[b]*Pharmaceutical Sciences Laboratory, Faculty of Science and Engineering, Åbo Akademi University, Turku 20520, Finland. E-mail: hongbo.zhang@abo.fi*
[c]*NHC Key Laboratory of Hearing Medicine (Fudan University), Shanghai, 200031, China*
[d]*Laboratory of Industrial Physics, Department of Physics and Astronomy, University of Turku, Turku 20500, Finland*
[e]*Stem Cell and Regenerative Medicine Lab, Beijing Institute of Radiation Medicine, Beijing 100850, China*
[f]*Turku Bioscience Centre, University of Turku and Åbo Akademi University, Turku 20520, Finland*
[g]*The First Affiliated Hospital of Wenzhou Medical University, Wenzhou, China*
†Electronic supplementary information (ESI) available. See DOI: https://doi.org/10.1039/d2nr04095f
‡These authors contributed equally to this work.

Secondly, most delivery particles are nanoscale and prepared by conventional batch methods. Due to the stepwise scaling up process, the synthesis is easily affected. This makes it difficult to achieve a mass of nanocarriers with the same structures or properties.[13] Thirdly, the possible off-target effect resulted from the lack of precise control over editing has severely constrained the application of current CRISPR/Cas9 systems, which may likely cause serious side effects, such as tumor.[14] Hence, the excavation of an efficient and precise CRISPR/Cas9 RNP delivery platform based on non-viral vectors is the premise.

Among many delivery systems, metal–organic frameworks (MOFs) assembled from metal ions and polydentate ligands already show great potential as a substrate for guest molecules.[15] Different biomolecules such as DNA, proteins, drugs, and other enzymes have been encapsulated into MOFs.[16,17] For example, by preparation of zeolitic imidazolate frameworks-8 (ZIF-8) utilizing the extremely mild conditions (aqueous solution), enzymes (including horseradish peroxidase, urease and pyrroloquinoline quinone-dependent glucose dehydrogenase) can be biomineralized *in situ* by generating defects in the ZIF-8 crystal during the synthesis process, denoted biomimetic mineralization.[18] Unlike traditional cargo loading methods, such as surface adsorption, non-covalent interaction and covalent connection, biomimetic mineralization strategy is able to *in situ* grow MOFs at the surface of biomolecules.[19,20] By this one-pot process, biomolecules are immobilized into MOFs, allowing for good protection of host biomolecules and high loading efficiency. Another attractive feature surrounding this strategy is the responsive collapse of the MOFs under specific situation (temperature, pH and *et al.*) to trigger the sufficient releasing of the encapsulated biomolecules.[21,22] However, biomineralization process using the traditional "bulk methods", which usually lacks precise control and has huge batch-to-batch difference in particle size distribution, cargo immobilization or release profiles seriously hinders their biological and medical applications. A recent and emerging technology, microfluidics, has become an alternative to conventional bulk methods for micro/nanoparticles preparation.[23–27] Accordingly, microfluidics is the nanotechnology that can manipulate fluids in microchannels with reduced reagent consumption and improved heat or mass transfer. This allows microfluidic devices to control synthesis parameters, leading to desired particle size and morphology together with reproducibility.[28] Until now, several uniform MOF nanostructures, including HKUST-1, UiO-66(Zr), MIL-88B, ZIF-8 and IRMOF-3, have been synthesized in microfluidic systems.[29–31] Besides, microfluidic devices are developed for the preparation of desirable characteristics of different nanoparticles (core–shell structures, functional surfaces or composite materials).

Here, we describe a microfluidic-assisted MOF based biomineralization strategy and utilized it for the efficient delivery and remote regulation of CRISPR/Cas9 RNP gene-editing. The strategy was performed by biomimetically growing of a thermal-responsive EuMOF onto photothermal template Prussian blue (PB) and encapsulating ribonucleoprotein (RNP) during the MOFs' crystallization process in microfluidic channels. This strategy was more time efficient than the bulk encapsulation process and allowed higher reproducibility of the encapsulation process, higher encapsulation efficiency (60%) and better protection for RNP in the presence of trypsin and SDS by simple adjusting of microfluidic parameters (flow rate or reactant concentration). Due to the high photothermal conversion ability of PB ($\eta$ = 34%) and thermo-responsive degradation of EuMOFs (($T \geq 37$ °C)), the nanocarrier offers an appealing avenue to achieve photo-controlled RNP release without bioactivity disruption. After cellular uptake, accelerating endosomal escape was observed in the NIR-irradiated group and higher editing efficiency was induced (40%, 48 h) than Lipofectamine CRISPRMAX (31%, 48 h) using the target GFP gene as model gene under calculation of mean fluorescent intensity. Moreover, the control of gene-editing activity can be programmed by exposure times adjusting, which showed higher editing efficiency (42%, three times and 47%, four times) than laser exposure twice. Sanger sequencing assay also proved the laser induced editing activity. As a proof-of-concept, this strategy here combined effective delivery and precise control of CRISPR/Cas9 RNP-based gene editing, showing its great potential for biomedical therapeutic applications.

## 2. Materials and methods

### 2.1. Materials and characterization

Potassium hexacyanoferrate(III) ($K_3[Fe(CN)_6]$, ACS reagent, ≥99.0%), guanosine 5′-monophosphate disodium salt hydrate (GMP, from yeast, ≥99.0%), europium(III) chloride hexahydrate ($EuCl_3{\cdot}6H_2O$, 99.9%), cell proliferation reagent (WST-1), paraformaldehyde (PFA, 95%) and 4′,6-diamidino-2-phenylindole (DAPI, nucleic acid staining) were purchased from Sigma-Aldrich. Polyvinylpyrrolidone (PVP, M.W. 8000) was purchased from Alfa Aesar by Thermo Fisher Scientific. Sulfo-Cyanine5.5 NHS ester (Cy5.5) was purchased from Lumiprobe GmbH. Alt-R® S.p. Cas9 Nuclease V3 and Alt-R® CRISPR-Cas9 sgRNA (5′-GGAGCGCACCATCTTCTTCA-3′) were purchased from Integrated DNA Technologies, Inc.

The morphology of the synthetic nanoparticles was evaluated by a TEM (JEOL 1400 Plus, USA). Elemental analysis of the nanoparticles was done using a field-emission SEM (Thermo Scientific Apreo S, The Netherlands) with an energy-dispersive X-ray spectrometer (EDS; Oxford Instruments UltimMax 100, United Kingdom). Particle size and size distrubrution were characterized by dynamic light scattering with a Zeta sizer Nano ZS (Malvern Instruments Ltd, UK). Zeta potential was recorded by Zetasizer Nano ZS using disposable folded capillary cells (DTS1070, Malvern, UK). Fourier-transform infrared spectroscopy (FTIR) spectra of solid samples were collected using a PerkinElmer spectrum two FT-IR spectrometer. The encapsulation and release process were measured using NanoDrop 2000c Fluorospectrometer (ThermoFisher, USA). The stability of Cas9 protein was determined using NanoDSF instrument: Prometheus NT.48 (NanoTemper). The confocal microscopy

images were performed by Zeiss LSM880 with Airyscan. Flow cytometry analysis was recorded using BD LSRFortessa Blues.

### 2.2. Sythesis of Prussian blue (PB)

The sythesis of PB was conducted according to the method by Yamauchi group.[22] Firstly, PVP (3 g) and $K_3[Fe(CN)_6]$ (226.7 mg) were dissolved into water (40 mL) to form a clear aqueous solution by magnetic stirring. Then 35 μL concentrated hydrochloric acid were added. The reaction solution was kept stirring for 30 min and then heated it to 80 °C. After 20 h aging, the production was collected by centrifugation and washed three times with deionized water and ethanol. The PB products were dispersed in water for further use.

### 2.3. Fabrication of microfluidic chip

The 3D microfluidic co-flow focusing chip was made by fabricating two borosilicate glass capillaries (World Precision Instruments Ltd, UK) on a glass slide. The two glass capillaries with outer diameter of around 1000 and 1500 μm, respectively, were named as inner and outer capillaries. In brief, one end of the inner capillary was tapered using a magnetic glass microelectrode horizontal needle puller (P-31, Narishige Co., Ltd, Japan), following by sandpaper (Indasa Rhynowet, Portugal) polishing until the cross-section became flattened. Then the inner tapered capillary was inserted into the outer capillary and coaxially aligned. After fixing them on the glass slide, one hypodermic needle was be situated to the outer capillary and sealed with transparent epoxy resin.

### 2.4. Preparation of PB@EuMOFs

**2.4.1 In microfluidic system.** The PB@EuMOFs core–shell nanoparticles were prepared using microfluidic co-flow device at room temperature. In general, PB and $Eu^{3+}$ were mixed together and kept stirring for 5 min to form one stable system by electrostatic interaction, which served as the inner fluid. The GMP aqueous solution was set as the outer fluid. These two fluids were separately pumped into the microfluidic chip. During this process, the inner fluid were focused by the outer continuous fluid. The flow rate of the different fluid was controlled by pumps (PHD 2000, Harvard Apparatus, USA). In this procedure, EuMOFs particle formed and coated outside of PB immediately. The resulting product was collected by centrifugation and washed with deioned water several times to remove any residues. In order to optimize and adjuste the physicochemical properties of the obtained core–shell nanostructures, several formulation parameters were assessed, such as the total flow rate of inner and outer fluids, the flow ratio between these two fluids, and the concentration of each reactant.

**2.4.2 In bulk method.** By comparation, we have prepared the PB@EuMOFs nanoparticles using a bulk method. In brief, the PB and $Eu^{3+}$ mixed solution was added dropwise into the GMP solution with the same concentration in microfluidic system.

### 2.5. Photothermal effect measurements

Different concentration of PB@EuMOFs (10, 20, 50 μg $mL^{-1}$) in 1.0 mL aqueous solution was prepared and transferred to transparent cuvettes. After that, NIR irridation (808 nm, 2 W $cm^{-2}$) was performed. Taking 1 min as time intervals, temperature of PB@EuMOFs solution with different concentrations was monitored using a digital non-contact infrared thermometer until the temperature reached maximum. The negative control group ($H_2O$, 1 mL) was also recorded under the same parameters. The photothermal conversion efficiency ($\eta$) can be calculated using the following formulas:

$$\eta = \frac{hA\Delta T_{max} - Q_s}{I(1 - 10^{-A_\lambda})} \quad (1)$$

In order to get the unknown value of $hA$, we introduced the ration of $\Delta T$ (temperature change) to $\Delta T_{max}$, which defined as $\Theta$:

$$\Theta = \frac{\Delta T}{\Delta T_{max}} \quad (2)$$

Then, $hA$ can be calculates as following:

$$hA = \frac{mC_p}{\tau} \quad (3)$$

where $\tau$ is the slop of the linear time data from the cooling period *vs.* $-\ln \Theta$ (Fig. S9†). $m$ is the mass of water and $C_p$ is the heat capacity of water.

### 2.6. Encapsulation and NIR-induced release of RNP

Cy5.5 labeled Cas9 has been used to evaluate the encapsulation efficiency and releasing capability of our MOFs-based nanocarrier. To perform the biomineralization process that encapsulates CRISPR/Cas9 RNP into the MOFs, the same microfluidic method with a little modification was adopted. Cas9 and sgRNA can be mixed in PBS at a molar ratio of 1 : 1 and incubated for 5 min to form RNP. Then the RNP were mixed with GMP in water at desired concentrations, which was selected as the outer fluid together. The rest of the steps remain exactly the same as the PB@EuMOFs nanoparticles. The encapsulating procedure was monitored by a meros high-speed digital microscope (Dolomit microfluidics), in which the inner fluid was focused by the outer continuous fluid. To achieve the best encapsulation degree and nanocarrier morphology, different reagent flow rates and concentrations of RNP complexes with MOFs precursors during the microfluidic encapsulation process have been adjusted. After centrifuging, the RNP that was not encapsulated into MOFs were found in the supernatant and assayed by using UV-vis spectrophotometer at wavelength of 678 nm. Both encapsulating efficiency (EE%) and capacity (EC%) were calculated using the following formula:

$$EE\% = \frac{A_i - A_f}{A_i} \times 100\% \quad (4)$$

$$EC = \frac{A_i - A_f}{A_{MOFs}} \quad (5)$$

The NIR-controlled release of the obtained RNP@PB@EuMOFs was studied upon radiation by the 808 nm laser. In brief, the collected RNP@PB@EuMOFs were dispersed into PBS and irradiated with NIR light for different

 

time periods. The amount of released RNP was operated by discarding the supernatant after centrifugation and replacing it with a new buffer at the specific time points. Then the releasing profiles was measured using UV-Vis spectrophotometer according to the absorption wavelength of Cy5.5. As control, the releasing behavior without NIR irradiation was also carried out under the same procedures.

### 2.7. Cell culture

Human cervical cancer cells introduced with green fluorescence protein genes (HeLa/GFP) were bought from Nordic BioSite Oy (Finland) and HeLa cells were generous gifts from Prof. Jukka Westermarck at Turku Bioscience Centre (Biocity, Finland). Both cell lines were cultured in a 37 °C incubator under 5% $CO_2$ and 90% humidity with complete growth medium: DMEM supplemented with 10%, v/v heat inactivated FBS, 1% penicillin/streptomycin solution, 0.5% nonessential amino acid, and 1% L-glutamine.

### 2.8. *In vitro* cellular toxicity test

To study cytotoxicity of prepared nanoparticles, WST-1 assay was utilized according to the manufacture's protocol. HeLa/GFP and HeLa cells were seeded into 96-well plate ($5 \times 10^3$ cell per well) one day before and then cultured in an incubator. Then the cell growth medium was replaced with a fresh medium containing different concentrations of PB@EuMOFs. 100 μL DMEM with 10 μL dimethyl sulfoxide (DMSO) was taken as positive control. After that, the plate was further incubated for an additional 48 h. During the incubating, two times of laser irradiation were conducted at 24 h and 48 h, in which the infrared thermometer was used to monitor and control the final temperature under 42 °C. After adding WST-1 reagent (10 μL) to each well, the cells were incubated at 37 °C for another 2 h. The absorbance was measured by a Varioskan Flash Multimode Reader (Thermo Scientific Inc., Waltham, MA, USA) at 440 nm. Five wells were read for each concentration and average absorbance reading were plotted.

### 2.9. *In vitro* cellular uptake study

For cellular uptake study, Cy5.5-doped PB@EuMOFs were used. HeLa/GFP cells were seeded into 24-well plate ($5 \times 10^4$ cells per well) and cultured overnight. PB@EuMOFs were dispersed into cell culture medium (50 μg $mL^{-1}$) and added to the wells (1 mL per well). After incubating under a selected time point (1, 2, 4, 6 h) at 37 °C, the cells were harvested and re-suspended in PBS for the flow cytometry analysis. For CLSM analysis, HeLa/GFP cells were seeded into confocal dishes ($18 \times 10^4$ cells per dish) and incubated with PB@EuMOFs (50 μg $mL^{-1}$, 2 mL). At a selected time point (1, 2, 4, 6 h), cells were washed with PBS, stained with DAPI (5 μg $mL^{-1}$, 2 mL) and further fixed with PFA (4%, 2 mL).

### 2.10. *In vitro* endosomal escape study

HeLa cells were seeded into confocal dishes ($18 \times 10^4$ cells per dish) and cultured overnight. The fresh-prepared PB@EuMOFs (with Cy5.5) were dispersed into cell culture medium and added to confocal dishes (50 μg $mL^{-1}$, 2 mL). At a selected time point (1, 2, 4 h), the cells were stained with Lysotracker Green (10 μM, 200 μL). After 2 h incubation at 37 °C, cells were washed with PBS, stained with DAPI (5 μg $mL^{-1}$, 2 mL) and further fixed with PFA (4%, 2 mL). For comparation, the corresponding dishes were subjected to 808 nm laser irradiation (2 W $cm^{-2}$, 50 s) before Lysotracker Green stain. Infrared thermometer was used to monitor the temperature of cell culture medium during laser exposing and control the temperature up to 42 °C. The following steps were same with that one without laser and observing the cells with CLSM.

### 2.11. *In vitro* GFP disruption assay

HeLa/GFP cells were seeded into 96-well plate ($4 \times 10^3$ cells per well) the day before particle adding. PB@RNP-EuMOFs were prepared fresh and added to the wells, leading to the final amount of Cas9 was 250 ng and sgRNA was 50 ng. After incubation, 808 nm laser irradiation (2 W $cm^{-2}$, 10 s) was performed at determined time points (two times: 4 h and 6 h; three times: 4 h, 6 h and 8 h; four times: 4 h, 6 h, 8 h and 10 h). Infrared thermometer was used to monitor the temperature during laser exposing and control the temperature within 42 °C. The cells were kept at 37 °C and incubated for 48 h. Afterwards, the cells were analyzed using fluorescence microscopy and GFP gene disruption efficiency was quantified by flow cytometry.

The genomic DNA after PB@RNP-EuMOFs transfection was collected using DNA extraction kit (Monarch® genomic DNA purification kit) following the manufacturer's instruction. After extraction, the GFP-targeted genomic locus was amplified by high fidelity PCR master mix using the following primers: GFP-F: GTAAACGGCCACAAGTTCAGC and GFP-R: CCTTGATGCCGTTCTTCGC and purified by gel extraction. The edited DAN was sequenced by Eurofins Genomics Germany GmbH.

### 2.12. Statistics

All of the data were shown as mean ± standard deviations (SD) and analyzed using the Student's *t*-test. The statistical significance between groups was indicated by $***p < 0.001$, $**p < 0.01$, and $*p < 0.05$, respectively.

## 3. Results and discussion

### 3.1. Microfluidic-assisted biomineralization of MOFs

In this work, Prussian blue (PB) nanocubes were prepared through a modified single precursor method according to previous reference.[22] Transmission electron microscopy (TEM) results indicated that the average particle size of the synthesized PB was about 100 nm (Fig. S1a†), which was slightly smaller than the detected value in dynamic light scattering (DLS) (Fig. S1b,† $d_{nm}$ = 147.5 nm, polydispersity index (PDI) = 0.148). Net surface charge (zeta potential) of PB (0.8 mg $mL^{-1}$) was −42.4 mV in deionized water due to the negatively charged cyanoferrate groups on the PB surface. Considering its regular morphology and charged surface, PB was used as the hard

template for biomineralization of MOFs. Here, a microfluidic co-flow focusing device was manufactured as shown in Fig. 1a. Before injecting the fluid 1 through the inner capillary, which had an inner diameter (ID) of 580 μm, PB (1.4 mg $mL^{-1}$) and $Eu^{3+}$ (10 mM) were mixed together by stirring to form a stable system through electrostatic interaction. The linker solution, guanosine monophosphate (GMP, 10 mM), was injected as fluid 2 through the outer capillary. The two fluids were then mixed at the orifice (80 μm) of the tapped capillaries, realizing the fast mixing and self-assembly of $Eu^{3+}$ and GMP to form the core–shell structured PB@EuMOFs at the interphase (Fig. 1a).[32] The particles were collected constantly from the outlet, followed by centrifugation and washing steps. In this case, the fine-shaped PB solid-state nanostructure allowed for a better control of EuMOFs (Fig. S1c†), in which the formed nuclei of EuMOFs were attached to the template before undergoing further growth, leading a positive surface charge of 10.1 mV. Composition of the particles was then analyzed with STEM EDS, confirming the initial Fe-rich PB nanocubes to obtain a Eu-containing MOF layer (Fig. S1d and e†).

The crystallization of MOFs in microfluidic device was a kinetic self-assembly process, which could react under reaction-diffusion (RD) environments.[33] Generally, RD condition generated inside microfluidic channels mimic the processes found in nature which were important for crystal structures changing.[34] In this condition, the width of the RD zone (where the diffusive mixing occurs) formed between two-reactant fluids can be precisely controlled. Here, we used pure water with different dyes to visualize this process (Fig. 2a). Thus, the microfluidic procedure allows tailoring the core–shell structure of the prepared PB@EuMOFs through the variation of RD conditions. We defined the two input fluids and their corresponding flow rates as fluidic 1: Q1 and fluidic 2: Q2. The flow rate ratio (FRR) was defined as the ratio of flow between Q2 and Q1. Fig. 2b displayed the TEM images of the prepared PB@EuMOFs using different FRR. In all cases, EuMOFs were immediately prepared at the liquid interface between $Eu^{3+}$ and GMP, whereas the core–shell structure showed significant differences under different FRR. When adjusting the FRR to 4, the average dimensions of formed EuMOFs was 30 nm and the EuMOFs layer outside of PB was thin and noncontinuous. This is reasonable since as the FRR increased at a constant flow rate, the width of RD zone at the interface between the two reagent streams decreased (Fig. 2a).[33] The RD decreasing led to diffusion-limited and kinetically controlled environments where the formation of out-of-equilibrium crystal was promoted. When we varied the FRR from 4 to 1, the size of EuMOFs enlarged due to the RD zone increasing. The final structure of EuMOFs in FRR 1 was coincident with the ones that were produced by simple reactant mixing in bulk method. In this condition, although PB was coated with EuMOFs, the layer was huge and unevenness. The size distribution clearly increased from FRR 4 to FRR 1 (Fig. S2a†), which was attributed to the generation of free EuMOFs in low flow rate. Obviously, the RD zone adjusting could be used as a microengineering tool to guide self-assembly, but no uniform core–shell structure was achieved in all FFR condition. Therefore, the concentration ratio of every reactants has became a matter of intense investigation with this microfluidic method. The reactant stoichiometric concentration ratio (PB : $Eu^{3+}$ : GMP)

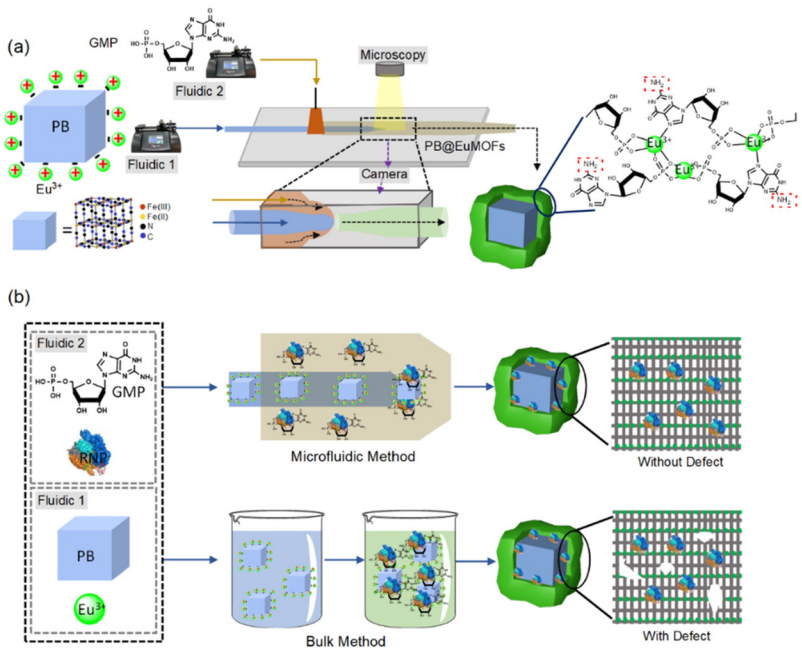


**Fig. 1** (a) Overview of 3D co-flow microfluidic device to prepare PB@EuMOF core–shell nanoparticles and structures of each reactant; (b) schematics of microfluidic and bulk synthesis methods of PB@RNP-EuMOFs composites. Fluidic 1 was the mixture of PB and $Eu^{3+}$ and fluidic 2 was the mixture of GMP and RNP.

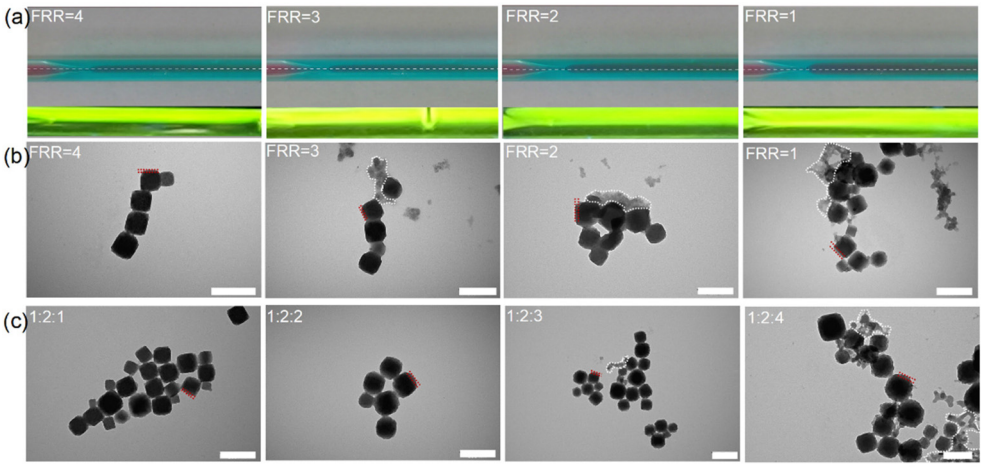


**Fig. 2** (a) Water fluid patterns in the microfluidic channel visualized by light microscope under different FRR. The RD zone was labeled with fluorescence dye and placed at the bottom of the corresponding FRR pictures; (b) TEM images of PB@EuMOFs prepared with different FRR, the concentration ratio of PB : Eu : GMP : Cas9 was 1 : 2 : 2.2; (c) TEM images of PB@EuMOFs prepared with different concentrations of reactants under the FRR = 3. The white dotted line was used to highlight the EuMOFs not growing on PB and the red dotted line was used to highlight the thickness of EuMOFs layers. Scale bar: 200 nm.

were optimized from 1 : 2 : 1 to 1 : 2 : 4 to guarantee rapid crystallization of EuMOFs, whereas no block happened to microfluidic channels. When we kept the FFR (FFR = 3) and concentration of PB in fluidic 1 constant, the concentration of $Eu^{3+}$ and GMP was the key factor to regulate the core–shell structure. In this case, $Eu^{3+}$ was concentrated around PB due to the electrostatic interaction. After injecting into the microchannel, the concentration of $Eu^{3+}$ had different gradients which was higher in the surrounding area of PB and lower in other places of the solution. As shown in Fig. 2c, defective EuMOFs layer was coated on PB at the concentration of 1 : 2 : 1 and more undesired isolated EuMOFs appeared at the concentration of 1 : 2 : 4. However, well-defined core–shell morphology could be observed when the concentration ratio was 1 : 2 : 2 and the EuMOFs shell was approximately 32 nm. The corresponding size distribution of every concentration ratio was given in Fig. S2b.† The findings clarify that the crystal framework of MOFs and the morphology of the prepared core–shell structures are significantly influenced by the flow conditions and concentration of different precursors in the microchannel.

### 3.2. Microfluidic-assisted biomineralization of CRISPR/Cas9 in MOFs

For CRISPR/Cas9 RNP encapsulation, the same microfluidic co-flow focusing device was utilized. According to the results above, the electrostatic interaction between $Eu^{3+}$ and PB played an important role in the formation of PB@EuMOF core–shell structures. Here, RNP was distributed to fluidic 2 that first mixed with GMP (Fig. 1b). And the results showed that the adding of RNP did not produce apparent interaction with GMP (Fig. S3†). The concentration of each precursor was 1 : 2 : 2 : 0.5 for PB : $Eu^{3+}$ : GMP : Cas9. After centrifugation and washing, RNP encapsulated PB@EuMOFs (PB@RNP-EuMOFs) with slight negative surface charge (−9.06 mV) was obtained, which showed no obvious morphology and size distribution changes and had good stability in different solutions (Fig. S4†). The encapsulating efficiency of RNP in the MOFs skeleton were performed using Cy5.5 conjugated Cas9 protein and determined by UV-vis absorption spectroscopy of Cy5.5 before and after encapsulation. As shown in Fig. S5,† the encapsulation efficiency and capacity were calculated to be 60% and 1.3 mg $g^{-1}$, respectively. Sametime, the possibility of precisely controlling of the solution mixing in microfluidic channels endowed the controllable and reproducible biomimetic process, which induced uniform particles size, low PDI and comparable encapsulation efficiency (Table 1).

To ascertain that RNP was indeed encapsulated into PB@EuMOFs but not absorbed on surface, the formed PB@RNP-EuMOFs were washed with polyvinylpyrrolidone (PVP, 8000 MW).[35] After centrifugation, the supernatant of PVP exchanging was measured using UV-vis absorption spectroscopy, and no obvious RNP was observed (Fig. S6†). Furthermore, confocal laser scanning microscopy (CLSM) images clearly revealed that Cy5.5 labeled RNP were well-dispersed throughout the entire MOFs skeleton (Fig. 3a). These data clearly demonstrated that RNP was indeed encapsulated

**Table 1** Batch-to-batch variation of PB@RNP-EuMOFs prepared by microfluidic and bulk methods

| Method | Batch | Particle size (d. nm) | PDI | RNP encapsulation efficiency (EE%) |
|---|---|---|---|---|
| Microfluidic | 1 | 147.5 | 0.116 | 58% |
| | 2 | 150.5 | 0.118 | 63% |
| | 3 | 146.5 | 0.180 | 61% |
| Bulk | 1 | 211.5 | 0.192 | 25% |
| | 2 | 186.2 | 0.179 | 39% |
| | 3 | 210.2 | 0.242 | 26% |

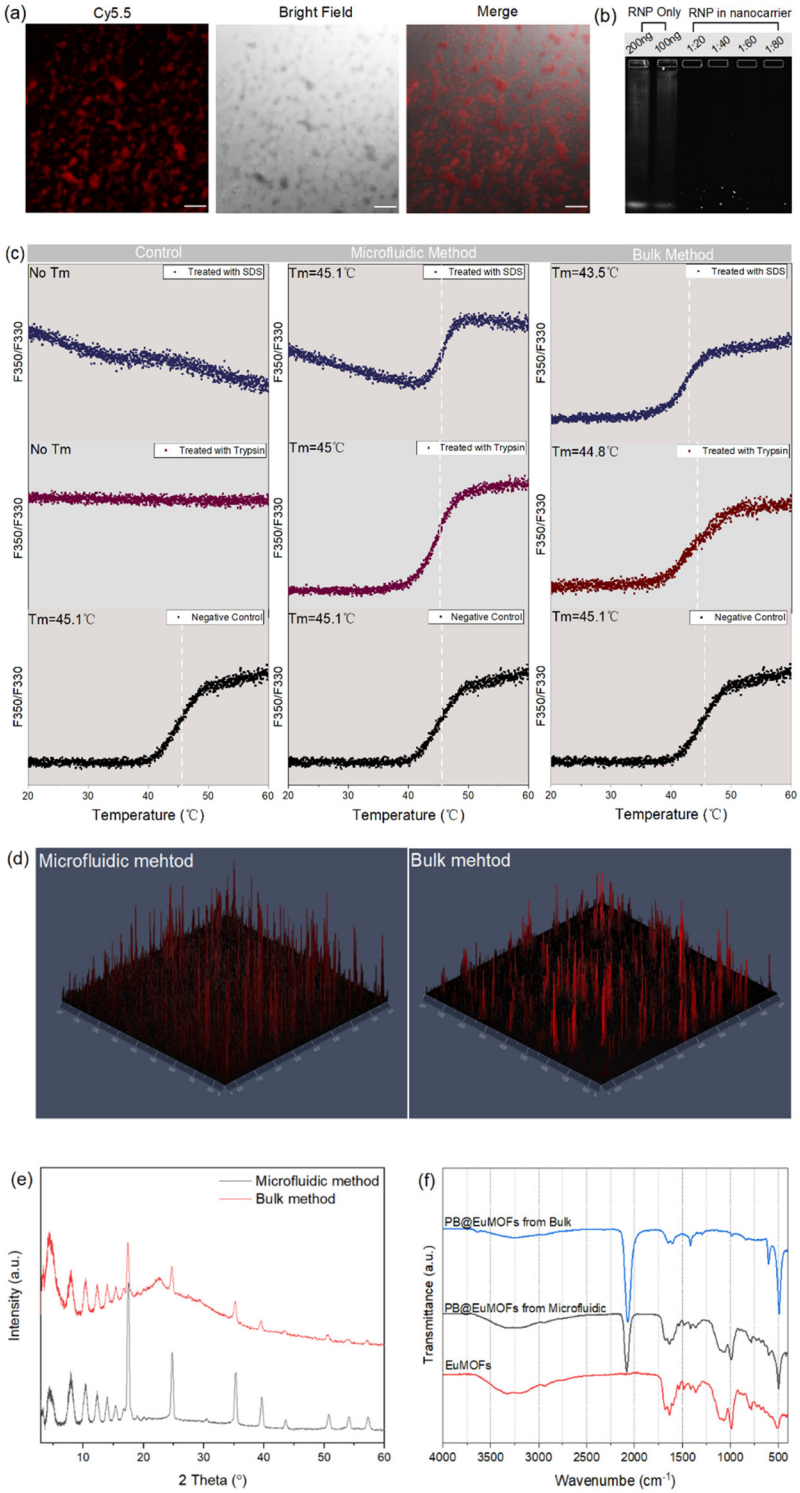


**Fig. 3** (a) CLSM images of microfluidic-prepared PB@RNP-EuMOFs obtained using Cas9 labelled with Cy5.5 (scale bar, 50 μm); (b) protein electrophoresis retardation assay of PB@RNP-EuMOFs at different mass ration of RNP and PB; (c) typical nanoDSF thermal unfolding curves of pure RNP released from microfluidic-prepared and bulk-prepared PB@RNP-EuMOFs. $T_m$ points were shown as vertical dotted lines; (d) 3D-CLSM profile of the distribution of Cy5.5-labeled RNP in PB@EuMOFs prepared by microfluidic (left) and bulk (right) methods; PXRD patterns (e) and FTIR analysis (f) of PB@RNP-EuMOFs prepared by different methods.

and evenly distributed into PB@EuMOFs nanostructures. Then, we determined the RNP retardation ability of PB@EuMOFs with protein electrophoresis. As shown in Fig. 3b, PB@EuMOFs could encapsulate CRISPR/Cas9 RNP and retarded its mobility at different mass ratios (RNP : PB = 1 : 20, 1 : 40, 1 : 60, 1 : 80). In nature, biomineralization processes are usually used to protect soft tissue from its ambient environment. The biological activity of Cas9 endonuclease and sgRNA is the key of RNP for its use in gene editing. This inspired us to examine whether our MOF coating could provide a similar barrier to protect the RNP. Here, trypsin and sodium dodecyl sulphate (SDS, 10%) were selected as extreme conditions that would normally cause protein inactivation. Nano differential scanning fluorimetry (nanoDSF) was used to determine the unfolding/denaturation of Cas9 protein by measuring the ratio of the fluorescence at 330 nm and 350 nm against temperature. The thermostability of protein was generally expressed by the thermal unfolding transition midpoint $T_m$ (°C). As shown in Fig. 3c, native RNP produced an obvious and robust melting point at 45 °C, which completely disappeared after treated by trypsin and SDS at room temperature for 5 min due to the denaturation of Cas9 in free RNP. Comparable, the released RNP from PB@RNP-EuMOFs composite retained almost the same $T_m$ (45 °C) under same treated condition with free RNP (Fig. 3c). This result exemplified a shielding function of the MOFs scaffold against different harsh environment.

For comparing, we prepared PB@RNP-EuMOFs nanostructures in bulk solution under same preparing condition as well (Fig. 1b). The encapsulation efficiency was calculated to be 30%, which was much less than that in microfluidic flow synthesis. It is important to note that both the morphology under TEM and particle distribution under DLS demonstrated a disorder core–shell structure of the bulk-prepared PB@RNP-EuMOFs (Fig. S7†). To validate whether the low encapsulation efficiency and poor morphology were because of the improper concentration ratio between the reactants, we synthesized PB@RNP-EuMOFs in bulk solution under different reaction conditions (Table S1†). All the products showed less than 40% of the encapsulation efficiencies, which suggested that the synthesis methods rather than the concentration ratio of reactants reduced the different encapsulation capability of RNP. It was able to obtain that the preparation of PB@RNP-EuMOFs by traditional bulk strategy induced the formation of nanocarriers with large particle sizes, high PDI and varying RNP encapsulation, resulting in a low batch repeatability (Table 1). Further, we monitored the RNP stability after release from bulk-prepared PB@RNP-EuMOFs by nanoDSF. The analysis of thermal unfolding/denaturation of released RNP clearly showed that both trypsin and SDS treatment induced the shift of $T_m$ towards lower values, from 45.1 to 44.8 °C for trypsin and from 45.1 to 43.5 °C for SDS (Fig. 3c). The result indicated that the outside MOFs shell in bulk method also showed its protection ability for encapsulated RNP, but slightly lower than that in the microfluidic method.

To investigate the fundamental reason of the different protection behavior of biomimetic MOFs in microfluidic flow and bulk solution synthesis, different characterizations were performed. The spatial distribution of RNP within PB@EuMOFs was determined using 2.5D-CLSM. Fig. 3d showed that RNP (with Cy5.5) molecules were more homogeneously distributed throughout PB@EuMOFs, as prepared by microfluidic flow than that prepared by bulk solution. Previous studies have proven that encapsulation process of biomolecules into MOFs might cause coordination defects in MOFs crystal structure.[35] Usually, this defect-producing behavior enables multimode pore diameter distribution in MOFs and therefore permits increased access of molecules that larger than pore size.[36] This was beneficial for enzyme-based catalysis, which facilitated substrate diffusion due to the defects in MOFs. Sametime, it might lead to slightly denaturation of inner biomolecules because of the access of some digestive enzyme or molecules. Therefore, we hypothesize that the reduced stability of RNP in bulk-prepared PB@EuMOFs was traceable by the crystal defects in MOFs. The crystal structure of PB@RNP-EuMOFs prepared by different methods are shown in Fig. 3e. PB@RNP-EuMOFs from microfluidic flow were more crystalline than PB@RNP-EuMOFs from bulk solution, indicating that the latter generated crystal defects, resulting in reduction in long-range order of the solid-state lattice.[37] Moreover, FTIR spectra showed a obvious decrease in intensity and increase of bandwidth (500–2000 $cm^{-1}$) on going from microfluidic-PB@RNP-EuMOFs to bulk-PB@RNP-EuMOFs (Fig. 3f), which was consistent with the reduced crystallinity and existence of crystal defects in PB@RNP-EuMOFs from bulk solution synthesis.

### 3.3. Photothermal conversion ability and NIR-triggered RNP release

Subsequently, the photothermal conversion ability of microfluidic-prepared PB@EuMOFs was investigated. PB displayed a strong absorption in the NIR region light, with the maximum absorption peak at *ca.* 720 nm, which was barely affected by EuMOFs surface growth (Fig. S8†). PB@EuMOFs aqueous solution with different concentrations (0, 10, 20 and 50 μg $mL^{-1}$) were separately exposed to 808 nm laser (2 W $cm^{-2}$, 10 min). As illustration in Fig. 4a, the temperature of PB@EuMOFs solution quickly increased and achieved a plateau of 42 °C under the concentration of 10 μg $mL^{-1}$ for 6 min. The maximum temperature generated by PB@EuMOFs increased dramatically with the increasing of concentration, which could be adjusted to 60 °C at 50 μg $mL^{-1}$. As a negative control, the temperature of pure water only went up by 3 °C after 10 min NIR irradiation. The final temperature under different concentration was recorded with an infrared thermal camera (Fig. 4b). Further, the photothermal conversion efficiency ($\eta$) was calculated according to the equations below (see ESI for details, Fig. S9†):[38]

$$\eta = \frac{hA\Delta T_{max} - Q_S}{I(1 - 10^{-A_\lambda})}$$

where $h$ is the heat transfer coefficient; $A$ is the surface area of container; $\Delta T_{max}$ is the temperature change at the maximum

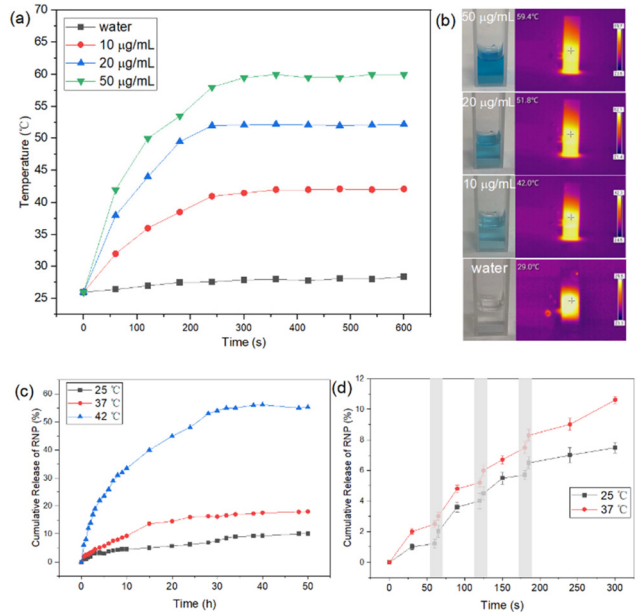


**Fig. 4** (a) Real-time temperature profiles of PB@EuMOFs at each concentration under 808 nm NIR irradiation (2 W $cm^{-2}$, 10 min); (b) photothermal images of PB@EuMOFs solution at various concentration recorded after 10 min laser exposing; (c) cumulative release profile of RNP from PB@RNP-EuMOFs under different temperature within 50 h; (d) NIR-triggered cumulative release profile of RNP from PB@RNP-EuMOFs at different temperature and different time points in grey boxes. Bars represent mean ± SD ($n$ = 3).

steady-state temperature; $Q_s$ is the heat associated with the light absorbance of water; $I$ is the laser power; $A_\lambda$ is the absorbance of PB@EuMOFs at 808 nm. Accordingly, the $\eta$ of PB@EuMOFs was determined to be 34%, demonstrating its good photothermal capability. The highest temperature that cells could tolerate is 42 °C, under which Cas9 protein could also maintain its nuclease activity. Therefore, we also explored the laser irradiation time that could stabilized the temperature at 42 °C with different concentration of PB@EuMOFs. As show in Fig. S10a,† under continuous irradiation, every concentration of PB@EuMOFs could be finely tuned to a narrow range of heating up to around 42 °C within a short time (<5 min). In addition, the irradiation time was also recorded for temperature to go from 37 °C to 42 °C (Fig. S10b†), which showed its potential for *in vivo* activation.

Subsequently, we investigated whether RNP release behavior could be manipulated through photothermal conversion of PB. Here, Cy5.5 labeled Cas9 protein was used. Due to the biomimetic encapsulation process, the effective release of RNP was based on the degradation of the MOF shell. Therefore, we measured the TEM images of prepared PB@RNP-EuMOFs after treating at different temperatures (25 °C, 37 °C and 42 °C). Results indicated that the morphology of outer EuMOFs suffers a more obvious collapse from 37 °C to 42 °C, whereas no structure degradation happen in the temperature of 25 °C (Fig. S11†). Subsequently, cumulative release profiles were determined and performed under different temperatures, which showed thermo-responsive RNP release behavior (Fig. 4c). The accelerated release percentage of RNP with a temperature rise from 25 °C to 42 °C increased from 16% to 55%, as recorded at 50 h after treatment. We then explored the RNP release behavior under NIR-induced photothermal heating by irradiating the release solution with 808 nm laser at different time points. Notably, the maximum temperature produced by laser exposure was no more than 42 °C. According to the results in Fig. S10,† the irradiation time for PB@RNP-EuMOFs at concentrations of 20 μg $mL^{-1}$ was 2 min from 25 °C to 42 °C and 1 min from 37 °C to 42 °C. As shown in Fig. 4d, the RNP release profile with laser-stimulus displayed a burst release phenomenon at both temperatures. The final release capabilities within 5 min were dramatically enhanced from 4% to 8% in 25 °C and from 5% to 11% in 37 °C, respectively, indicating that the photothermal conversion effect of PB@EuMOFs could exactly trigger the RNP release.

### 3.4. *In vitro* biocompatibility, intracellular uptake and endosomal escape

As an ideal delivery nanoparticle for RNP, its cytotoxicity should be minimized. To determine the biocompatibility of PB@EuMOFs, WST-1 assay was conducted in HeLa and HeLa/GFP cells. As shown in Fig. 5a, PB@EuMOFs exhibited low cytotoxicity in both cells, in which more than 90% of the cell

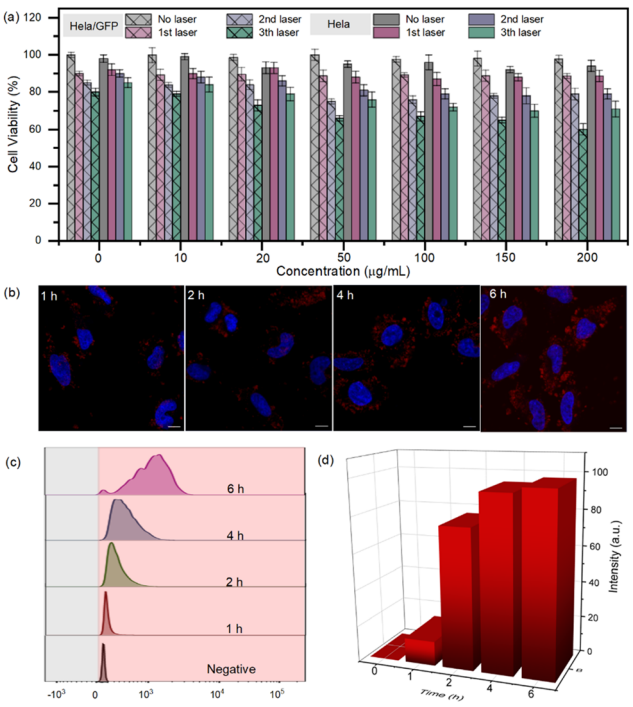


**Fig. 5** (a) Cell viability of HeLa and HeLa/GFP cells treated with different concentration of PB@EuMOFs and laser irradiation (808 nm, 2 W $cm^{-2}$) after 48 h incubation ($n$ = 6). Cellular uptake of Cy5.5-doped PB@EuMOFs after 1, 2, 4 and 6 h incubation detected by CLSM (b) and flow cytometry (c). The scale bar indicates 10 μm. (d) PB@EuMOFs-positive cell rates after 1, 2, 4 and 6 h incubation calculated from flow cytometry result.

viability were retained even at high particle' concentrations of 200 μg $mL^{-1}$. Simultaneously, the impact of PB@EuMOFs on cell viability under laser irradiation was also conducted to make sure its biosafety for RNP-based gene editing. Among laser irradiation, the temperature of cell culture medium in different concentrations was monitored using infrared thermal camera and controlled within 42 °C. After three cycles of irradiation, both type of cells showed high cell viability (>60%) (Fig. 5a). Flow cytometry analysis of the treated cells with three times irritation displayed similar cellular morphology with the control group (Fig. S12†). These results indicated that the prepared PB@EuMOFs were safe for cells even at relatively high concentration and with laser irridation. To further examine the time-dependent cell uptake of PB@EuMOFs, the CLSM images of HeLa/GFP cells incubated with PB@EuMOFs at different time points were taken. Cy5.5 dye with red fluorescence was encapsulated into the nanoparticles during MOFs shell formation. As shown in Fig. 5b, the red signal from PB@EuMOFs increased gradually with time. Fig. 5c shows the representative flow cytometry histogram plots, which reflected a high-efficiency in cellular uptake of PB@EuMOFs. The positive cells reaction with PB@EuMOFs was calculated to be 97.5% after 6 h of incubation (Fig. 5d). Taken together, these results confirmed that PB@EuMOFs could penetrate cell membranes effectively to deliver payloads into cells.

As nanoparticle-based delivery platforms are usually taken up by endocytosis, efficient endosomal escape is an essential prerequisite to accomplish gene editing with CRISPR/Cas9. To investigate to which degree the synthesized nanostructures

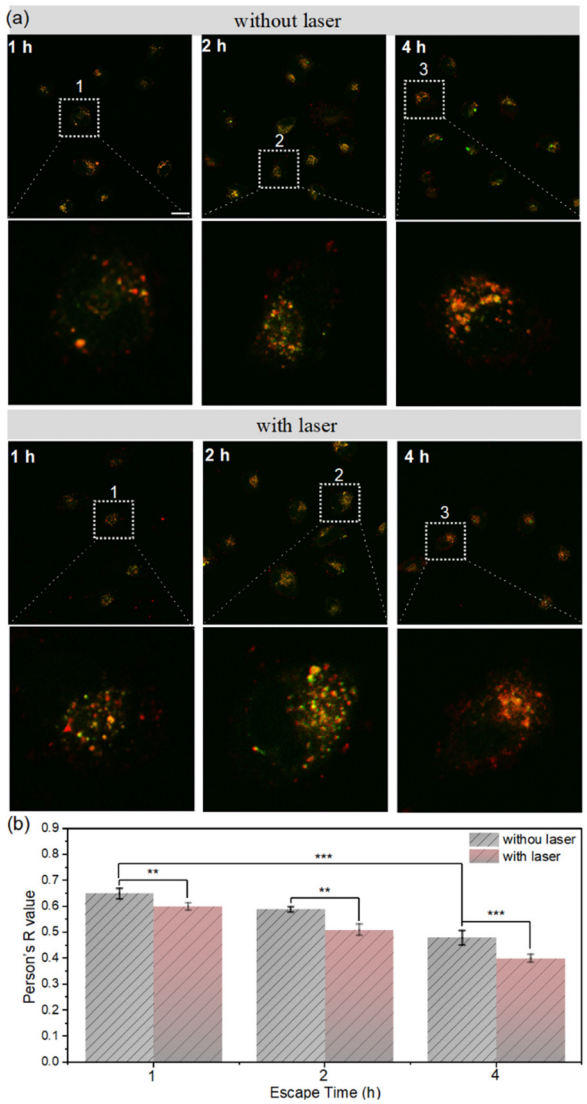


**Fig. 6** Endosomal escape images detected by CLSM (a) and Person's *R* value calculated by ImageJ (b) of PB@EuMOFs treated HeLa cells after 1, 2 and 4 h incubation. Endosomes were stained with Lysotracker Green and PB@EuMOFs was labeled with Cy5.5 (red). Statistical analysis was determined using *T*-test ($n$ = 3, ***$P$ < 0.001, **$P$ < 0.01, *$P$ < 0.05). Scale bar: 20 μm.

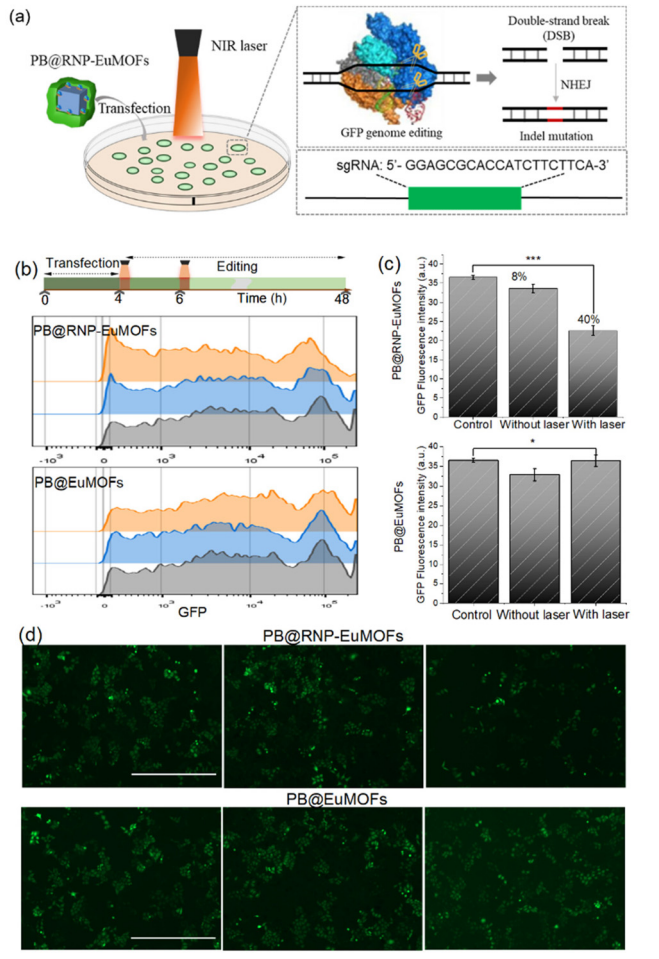


**Fig. 7** (a) Illustration of NIR programmable gene editing activation mediated by PB@RNP-EuMOFs. GFP gene editing efficiency of PB@EuMOFs and PB@RNP-EuMOFs in HeLa/GFP cells under the condition with and without laser irritation detected by flow cytometry (b), GFP fluorescence intensity calculated from flow cytometry results (c) and fluorescence microscopy (d), scale bar: 1000 μm ($n$ = 3, ***$p$ < 0.001 and *$p$ < 0.05 *versus* control).

were able to escape endosomes, Cy5.5-doped PB@EuMOFs were incubated with HeLa cells and the endosomes of the cells were stained with LysoTracker Green. CLSM images (Fig. 6a) exhibited colocalizations (yellow signals) of PB@EuMOFs and endosomes after 1 h incubation, while turned to clear signals separation in 4 h. Pearson's *R* value calculated using Coloc 2 method was decreased from 0.65 at 1 h to 0.48 at 4 h, indicating the successful endosomal escape of PB@EuMOFs (Fig. 6b). This is thought to be mainly owing to the proton sponge effect of $-NH_2$ in EuMOFs. PB@EuMOFs nanoparticles were also explored in parallel to study the effect of laser irradiation on the endosomal escape process. The 808 nm laser irradiation was applied after 1 h incubation since we assumed that the particles had high accumulation in endosomes at that time point. As shown in Fig. 6a, a lot more PB@EuMOFs escaped from endosomes after laser irradiation. The final Person's *R* value was 0.4 after 6 h incubation for the laser treated group (Fig. 6b). Obviously, the red signal is more evenly distributed after laser irradiation, which indicated that the photothermal conversion effect of PB@EuMOFs could facilitate its escape from endosomes.

### 3.5. NIR programmable gene editing

After establishing the efficiency of PB@EuMOFs in CRISPR/Cas9 RNP delivery, we also evaluated the gene editing ability of the nanocarriers for targeted DNA cleavage and NHEJ-induced repair. We used sgRNA to target the coding region of green fluorescent protein (GFP) in HeLa/GFP cells, which could result in shifting of reading frame and consequently preventing the expression of GFP (Fig. 7a).[39] The targeting sequence in sgRNA was 5′-GGAGCGCACCATCTTCTTCA-3′. To perform it, HeLa/GFP cells were incubated with PB@EuMOFs and PB@RNP-EuMOFs for 48 h. As shown in Fig. 7b and c, the intensity of GFP fluorescence in HeLa/GFP cells decreased by 40% with the laser irradiation in the group of PB@RNP-EuMOFs. Nevertheless, no obvious GFP fluorescence change was observed in the cells that were treated with PB@RNP-EuMOFs without laser, suggesting the controllable gene editing due to the photothermal-responsive release characteristics of CRISPR/Cas9 RNP from the PB@EuMOFs. In the group of PB@EuMOFs only, there was negligible GFP knockout even under laser irradiation. Fluorescence microscopy images also confirmed the decrease in GFP signals after PB@RNP-EuMOFs incubation and laser exposure (Fig. 7d). The gene knockout efficiency was compared to the commercial transfection reagent Lipofectamine CRISPRMAX according to the manufacture's protocol. The amount of Cas9/sgRNA used was 100 ng/20 ng. The editing efficacy of Lipofectamine CRISPRMAX for HeLa/GFP cells was calculated to be 31% after 48 h (Fig. S13†), which was closely similar to the results treated of PB@RNP-EuMOFs + NIR treatment. Despite this, our delivery system still had significant advantages in terms of photo-controlled gene editing, since there was no obvious controllable behaviour taking place in Lipofectamine CRISPRMAX.

After the successful demonstration of NIR-induced gene editing, we next explored whether the degree of GFP knockout could be controlled by such a modality. Different laser times

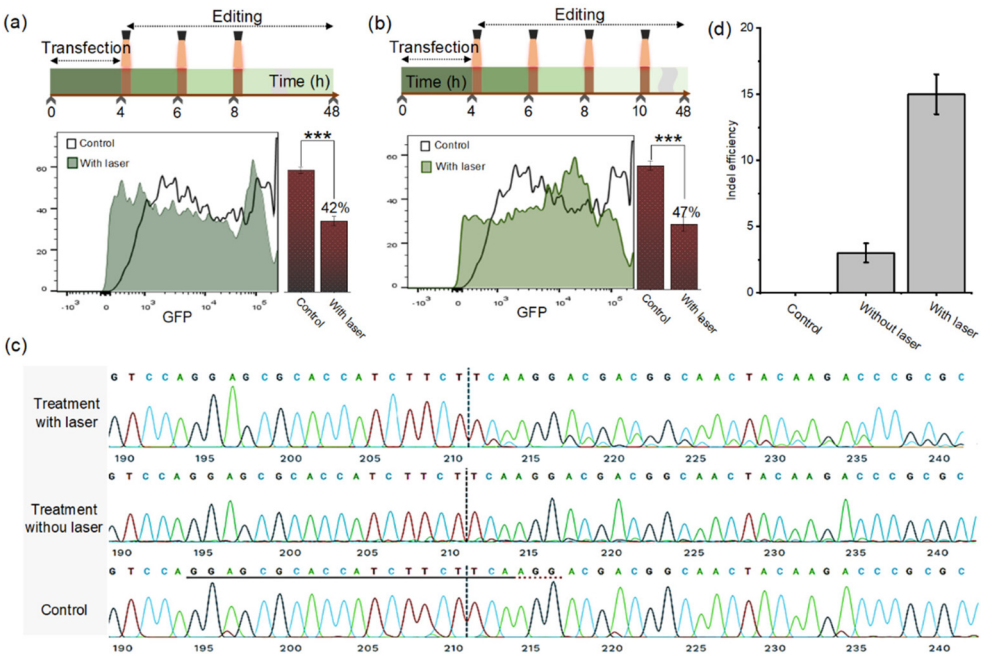


**Fig. 8** PB@RNP-EuMOFs-mediated photo-control of GFP editing efficiency detected by flow cytometry under laser irridation with tree times (a) and four times (b). The transfection, irradiation and gene-editing processes were illustrated and the laser irradiation time should be controlled temperature does not exceed 42 °C. (c) Sanger sequencing results of PCR amplicon of the targeted sites after treatment with PB@RNP-EuMOFs with and without laser irridation. The overlapping peaks indicates that there are at least two different fragments, and the more peaks appearing under the same peak shape means more fragments. (d) Indel efficiency results of PCR amplicon by ICE after treatment with PB@RNP-EuMOFs with laser irridation four times. The *N* indicates a random insertion of a base (($n$ = 3, ***$P$ < 0.001 *versus* control).

were applied to HeLa/GFP cells post-treated by PB@RNP-EuMOFs and the editing efficiency of GFP was compared after 48 h incubation. As reflected by Fig. 8a, the intensity of GFP fluorescence decreased more (efficiency: 42%) following three times irradiation compared the result in Fig. 7b and c, where laser exposure was applied only twice. The irradiation time points were set as 4, 6 and 8 h after particles incubation. GFP expression was further downregulated and knockout efficiency reached 47% after laser exposure for four times (4, 6, 8, 10 h) (Fig. 8b). Corresponding fluorescence microscopy images are shown in Fig. S14,† showing remarkable reduction in green signal of GFP. In addition, to get a more visual and accurate understanding of the knockout, the Sanger sequencing assay of four-time irradiation group was performed. The sequence results were analyzed by short for inference of CRISPR Edits (ICE) tools. As shown in Fig. 8c, more miscellaneous peaks at the target site of PCR fragments appeared and the indel efficiency was calculated to be 15%, which was much higher than that in the treatment group without laser (3%) (Fig. 8d). The relative contribution (Fig. S15†) shows single-nucleotide insertions were the indel patterns at the target site, which changed open reading frame (ORF) and caused premature termination of translation at a new nonsense or chain termination codon. Collectively, the photothermal conversion effect of PB@RNP-EuMOFs have successfully triggered controllable gene editing *in vitro*.

## 4. Conclusions

In conclusion, a microfluidic-assisted biomineralization strategy of MOFs was constructed and utilized for efficient CRISPR/Cas9 RNP delivery and NIR-responsive gene-editing remote control. By simply adjusting the microfluidic parameters (flow rate and reactant concentration), thermo-responsive degraded EuMOFs could regularly grow on photothermal conversion template PB, and encapsulate RNP during EuMOF crystallization. Due to the combination of microfluidic technology and MOF-based biomineralization, RNP encapsulated nanocarriers (PB@RNP-EuMOFs) possessed more uniform particle distribution, higher encapsulation efficiency and better RNP protect capacity than tradition bulk nanoprecipitation method that had more crystal defects in the MOF structure. Under NIR laser irradiation, the heat induced by PB conversion could induce the degradation of EuMOFs, resulting in promoted endosomal escape and effective RNP release. In addition, our strategy successfully down-regulated the expression of targeted GFP gene *via* NIR light-activated gene-editing *in vitro*. The gene-editing activity could be programmed by exposure times adjusting, which shows higher editing efficiency in correlation to longer exposure times (42%, three times and 47%, four times). Taken together, this study provides a proof-of-concept of microfluidic technology in MOFs biomineralization and its application in precise CRISPR/Cas9 gene-editing. This strategy may offer a useful tool for CRISPR/Cas9 gene-editing-based precise biomedical therapy in the near future.

## Author contributions

Xiaoyu Xu: project design, experiment operation, data collection and analysis, original manuscript writing; Chang Liu: microfluidic chip preparation, data analysis and figures drawing; Shenyi Wang: data analysis and manuscript reviewing; Jiali Wang: data collection and analysis; Junnian Zhou: cell experiment supervision and data analysis; Oliver Koivisto: DNA sequencing experiment operation and data collection; Jessica M. Rosenholm: supervision, resources and manuscript reviewing; Yilai Shu: supervision, resources, manuscript reviewing, and funding acquisition; Hongbo Zhang: supervision, resources, manuscript reviewing, and funding acquisition.

## Conflicts of interest

The authors declare that they have no known competing financial interests or personal relationships that could have appeared to influence the work reported in this paper.

## Acknowledgements

Confocal imaging and flow cytometry were performed at the Cell Imaging and Cytometry core (CIC) at the Turku Bioscience Centre, which is supported by Biocenter Finland. We thank the Electron Microscopy Laboratory, Institute of Biomedicine, University of Turku, and Biocenter Finland. SEM-EDS imaging was carried out using the facilities of Materials Analysis Research Infrastructure (MARI) at the Department of Physics and Astronomy, University of Turku. This work is supported by Academy of Finland (grant no. 328933), project (347897), Finland-China Network in Food and Health international pilot project (**https://fcfh.utu.fi/**) funded by the Finnish Ministry of Education and Culture, Sigrid Jusélius Foundation, National Natural Science Foundation of China (82171148), National Key R&D Program of China (2020YFA0908201), and China Postdoctoral Science Foundation (2021M700830). This research is also part of the activities of the Academy of Finland-funded strategic research profiling are Solutions for Health (336355) and InFLAMES Flagship (337531) projects from Academy of Finland.

## References

1 L. Cong, F. A. Ran, D. Cox, S. L. Lin, R. Barretto, N. Habib, P. D. Hsu, X. B. Wu, W. Y. Jiang, L. A. Marraffini and F. Zhang, *Science*, 2013, **339**, 819–823.
2 J. Liu, J. Chang, Y. Jiang, X. D. Meng, T. M. Sun, L. Q. Mao, Q. B. Xu and M. Wang, *Adv. Mater.*, 2019, **31**, 1902575.
3 W. Q. Cai, T. L. Luo, L. Q. Mao and M. Wang, *Angew. Chem., Int. Ed.*, 2021, **133**, 8679–8689.

4 C. F. Xu, G. J. Chen, Y. L. Luo, Y. Zhang, G. Zhao, Z. D. Lu, A. Czarna, Z. Gu and J. Wang, *Adv. Drug Delivery Rev.*, 2021, **168**, 3–29.
5 X. Y. Xu, O. Koivisto, C. Liu, J. N. Zhou, M. Miihkinen, G. Jacquemet, D. Q. Wang, J. M. Rosenholm, Y. L. Shu and H. B. Zhang, *Adv. Ther.*, 2021, **4**, 2000072.
6 G. J. Chen, A. A. Abdeen, Y. Y. Wang, P. K. Shahi, S. Robertson, R. S. Xie, M. Suzuki, B. R. Pattnaik, K. Saha and S. Q. Gong, *Nat. Nanotechnol.*, 2019, **14**, 974–980.
7 S. Zhang, J. T. Shen, D. L. Li and Y. Y. Cheng, *Theranostics*, 2021, **11**, 614–648.
8 R. M. Martin, K. Ikeda, M. K. Cromer, N. Uchida, T. Nishimura, R. Romano, A. J. Tong, V. T. Lemgart, J. Camarena, M. Pavel-Dinu, C. Sindhu, V. Wiebking, S. Vaidyanathan, D. P. Dever, R. O. Bak, A. Laustsen, B. J. Lesch, M. R. Jakobsen, V. Sebastiano, H. Nakauchi and M. H. Porteus, *Cell Stem Cell*, 2019, **24**, 821–828.
9 W. J. Sun, W. Y. Ji, J. M. Hall, Q. Y. Hu, C. Wang, C. L. Beisel and Z. Gu, *Angew. Chem., Int. Ed.*, 2015, **54**, 12029–12033.
10 J. A. Zuris, D. B. Thompson, Y. Shu, J. P. Guilinger, J. L. Bessen, J. H. Hu, M. L. Maeder, J. K. Joung, Z. Y. Chen and D. R. Liu, *Nat. Biotechnol.*, 2015, **33**, 73–80.
11 W. H. Zhou, H. D. Cui, L. M. Ying and X. F. Yu, *Angew. Chem., Int. Ed.*, 2018, **57**, 10268–10272.
12 C. A. Lino, J. C. Harper, J. P. Carney and J. A. Timlin, *Drug Delivery*, 2018, **25**, 1234–1257.
13 J. M. Wang and Y. J. Song, *Small*, 2017, **13**, 1604084.
14 L. Li, Z. Yang, S. J. Zhu, L. C. He, W. P. Fan, W. Tang, J. H. Zou, Z. Y. Shen, M. R. Zhang, L. G. Tang, Y. L. Dai, G. Niu, S. Hu and X. Y. Chen, *Adv. Mater.*, 2019, **31**, 1901187.
15 W. B. Liang, P. Wied, F. Carraro, C. J. Sumby, B. Nidetzky, C. K. Tsung, P. Falcaro and C. J. Doonan, *Chem. Rev.*, 2021, **121**, 1077–1129.
16 M. X. Wu and Y. W. Yang, *Adv. Mater.*, 2017, **29**, 1606134.
17 J. Yang and Y. W. Yang, *Small*, 2020, **16**, 1906846.
18 K. Liang, R. Ricco, C. M. Doherty, M. J. Styles, S. Bell, N. Kirby, S. Mudie, D. Haylock, A. J. Hill, C. J. Doonan and P. Falcaro, *Nat. Commun.*, 2015, **6**, 1–8.
19 K. Chen and C. D. Wu, *Coord. Chem. Rev.*, 2019, **378**, 445–465.
20 S. M. Huang, X. X. Kou, J. Shen, G. S. Chen and G. F. Ouyang, *Angew. Chem., Int. Ed.*, 2020, **59**, 8786–8798.
21 S. K. Alsaiari, S. Patil, M. Alyami, K. O. Alamoudi, F. A. Aleisa, J. S. Merzaban, M. Li and N. M. Khashab, *J. Am. Chem. Soc.*, 2018, **140**, 143–146.
22 D. D. Wang, J. J. Zhou, R. H. Chen, R. H. Shi, G. Z. Zhao, G. L. Xia, R. Li, Z. B. Liu, J. Tian, H. J. Wang, Z. Guo, H. B. Wang and Q. W. Chen, *Biomaterials*, 2016, **100**, 27–40.
23 Y. Wang, L. J. Li, H. M. Liang, Y. L. Xing, L. T. Yan, P. C. Dai, X. Gu, G. M. Zhao and X. B. Zhao, *ACS Nano*, 2019, **13**, 2901–2912.
24 Y. L. Balachandran, X. Li and X. Jiang, *Nano Lett.*, 2021, **21**, 1335–1344.
25 X. Li, M. Zha, Y. Li, J. S. Ni, T. Min, T. Kang, G. Yang, H. Tang, K. Li and X. Jiang, *Angew. Chem., Int. Ed.*, 2020, **59**, 21899–21903.
26 J. Sun, L. Zhang, J. Wang, Q. Feng, D. Liu, Q. Yin, D. Xu, Y. Wei, B. Ding, X. Shi and X. Jiang, *Adv. Mater.*, 2015, **27**, 1402–1407.
27 X. Y. Li, Q. Feng and X. Y. Jiang, *Adv. Healthcare Mater.*, 2019, **8**, 1900672.
28 D. F. Liu, H. B. Zhang, F. Fontana, J. T. Hirvonen and H. A. Santos, *Lab Chip*, 2017, **17**, 1856–1883.
29 M. Faustini, J. Kim, G. Y. Jeong, J. Y. Kim, H. R. Moon, W. S. Ahn and D. P. Kim, *J. Am. Chem. Soc.*, 2013, **135**, 14619–14626.
30 J. C. Cui, N. Gao, X. P. Yin, W. L. Zhang, Y. Liang, L. Tian, K. Zhou, S. Q. Wang and G. T. Li, *Nanoscale*, 2018, **10**, 9192–9198.
31 G. Y. Jeong, R. Ricco, K. Liang, J. Ludwig, J. O. Kim, P. Falcaro and D. P. Kim, *Chem. Mater.*, 2015, **27**, 7903–7909.
32 F. Duan, X. C. Feng, X. J. Yang, W. T. Sun, Y. Jin, H. F. Liu, K. Ge, Z. H. Li and J. C. Zhang, *Biomaterials*, 2017, **122**, 23–33.
33 M. Rubio-Martinez, I. Imaz, N. Domingo, A. Abrishamkar, T. S. Mayor, R. M. Rossi, C. Carbonell, A. J. deMello, D. B. Amabilino, D. Maspoch and J. Puigmarti-Luis, *Adv. Mater.*, 2016, **28**, 8150–8155.
34 M. Gonidec and J. Puigmarti-Luis, *Crystals*, 2019, **9**, 12.
35 G. S. Chen, X. X. Kou, S. M. Huang, L. J. Tong, Y. J. Shen, W. S. Zhu, F. Zhu and G. F. Ouyang, *Angew. Chem., Int. Ed.*, 2020, **59**, 2867–2874.
36 C. Hu, Y. X. Bai, M. Hou, Y. S. Wang, L. C. Wang, X. Cao, C. Chan, H. Sun, W. B. Li, J. Ge and K. N. Ren, *Sci. Adv.*, 2020, **6**, eaax5785.
37 X. C. Kang, K. Lyu, L. L. Li, J. N. Li, L. Kimberley, B. Wang, L. F. Liu, Y. Q. Cheng, M. D. Frogley, S. Rudic, A. J. Ramirez-Cuesta, R. A. W. Dryfe, B. X. Han, S. H. Yang and M. Schroder, *Nat. Commun.*, 2019, **10**, 1–10.
38 Y. L. Liu, K. L. Ai, J. H. Liu, M. Deng, Y. Y. He and L. H. Lu, *Adv. Mater.*, 2013, **25**, 1353–1359.
39 M. Hansen-Bruhn, B. E. F. de Avila, M. Beltran-Gastelum, J. Zhao, D. E. Ramirez-Herrera, P. Angsantikul, K. V. Gothelf, L. F. Zhang and J. Wang, *Angew. Chem., Int. Ed.*, 2018, **57**, 2657–2661.

 